coatings

MDPI

Article

Effect of Layer Thickness Ratio on the Roof Thermal Performance of Bilayer Waterborne Acrylic Coatings with a Barium Sulfate Reflective Topcoat and a Silica Aerogel Insulating Basecoat

Lingyu Jia *, Jianhua Ma and Jingke Xu

School of Intelligent Transportation and Intelligent Construction Engineering, Huanghe Jiaotong University, Jiaozuo 454950, China
* Correspondence: smliegod1992@163.com

Abstract

Reflective and insulating fillers are often combined in roof coatings, but the benefit attributed to their arrangement depends on optical properties, thickness constraints, and comparator selection. This study examines that dependence using an integrated optical–thermal evaluation framework for a waterborne acrylic bilayer with a barium sulfate reflective topcoat and a silica aerogel insulating basecoat. An optical saturation relationship is combined with transient one-dimensional heat conduction through a concrete roof at a nominal total coating thickness of 2.0 mm. The lowest daily positive inward heat gain among the original twelve allocations is 206.34 Wh m^{-2} at a reflective fraction of 0.35, compared with 219.76 Wh m^{-2} for the reflector-only reference. A finer fraction grid places the reference minimum at 0.335, with only a 0.013% difference from 0.35. A joint sensitivity assessment of eight bounded inputs across 512 parameter combinations gives minimizing fractions from 0.175 to 0.625. At a fixed fraction of 0.35, the paired benefit has 5th–95th percentiles across the investigated conditions of −1.00% to 6.07%, and is negative in 51 scenarios. Equal-optics controls eliminate the apparent effect of reversing the layers. Distributed coating storage changes the reference benefit from 6.11% to approximately 6.00%. These findings provide a systematic basis for optimizing the thickness allocation of bilayer reflective–insulating coatings by integrating optical saturation, thermal resistance, and parameter uncertainty. The proposed framework offers quantitative guidance for coating configuration design and establishes a foundation for subsequent experimental verification and practical applications.

Keywords: bilayer coating; barium sulfate; silica aerogel; layer thickness ratio; roof heat transfer

Check for updates

Academic Editor: Shadi Houshyar

Received: 4 October 2026
Revised: 7 November 2026
Accepted: 16 November 2026
Published: 18 November 2026

Copyright: © 2026 by the authors. Licensee MDPI, Basel, Switzerland. This article is an open access article distributed under the terms and conditions of the Creative Commons Attribution (CC BY) license.

1. Introduction

The exterior finish of a roof determines how much incident solar radiation is absorbed before heat enters the envelope. This boundary condition can be modified without replacing the underlying structure, making reflective coatings relevant to roof refurbishment. Nevertheless, a low exterior surface temperature is not a sufficient measure of building performance. The heat transmitted to occupied space also depends on substrate thickness, thermal storage, indoor conditions, and the timing of solar exposure. Recent experimental and heat-transfer investigations have therefore evaluated radiative cooling roofs through building energy balances and transient heat-transfer models rather than through a single surface-temperature difference [1–3]. This distinction is central to the present work: the

quantity to be minimized is positive inward heat gain at the room-side boundary, with surface temperature retained as a diagnostic variable.

Reflectance must also be considered over a service period. Field observations of aerogel-based and conventional reflective roof coatings show that aging, soiling, and cleaning can change thermal performance appreciably [4]. A coating with a favorable initial optical response may consequently provide a smaller sustained benefit than its first exposure suggests. At the material level, adding silica aerogel can reduce the conductivity of a polymer-rich coating, although the resulting performance depends on loading, dispersion, pore preservation, and binder penetration [5]. These mechanisms operate at different locations: reflection acts mainly near the exposed surface, whereas conductive resistance is accumulated through the thickness. A uniform blend is therefore not necessarily the most efficient arrangement, but a layered arrangement must be evaluated against controls that separate composition from geometry.

Bilayer radiative cooling architectures are already established research directions. Thin scattering coatings, thermoplastic polyurethane bilayers, and porous–dense structures have been investigated experimentally [6–8], while gradient particle distributions have been studied through optical modeling and measurement [9]. These studies address architecture, scattering, or functional performance using their own materials and conditions. The present study applies established optical and conduction relationships to a narrower allocation question: how strongly does a preferred layer fraction depend on constitutive parameter variation when total thickness is constrained? Its specific methodological contribution is to combine paired input propagation, equal-optics controls, and the assessment of spatial–temporal resolution and parameter-dependent design ranges. The focus is on integrating established optical and heat-transfer relationships into a reproducible thickness-allocation assessment.

Waterborne acrylic provides a practical common binder for examining this question. It allows the two layers to be formulated within the same polymer family, reducing one source of chemical incompatibility without eliminating the need to test intercoat adhesion. Hydrophobic silica aerogel in acrylic coatings has been studied experimentally and through models that account for resin intrusion [10]. Functionally graded aerogel coatings extend this interest from composition to spatial organization [11]. Related investigations of modified aerogel in waterborne polyurethane and secondary encapsulation strategies illustrate the importance of interface compatibility and water protection [12,13]. These studies motivate the present material choices; their reported material properties provide a comparative context for selecting and assessing the coating parameters.

Reflective cooling and low conductivity can coexist, but their roles should not be conflated. Calcium-silicate/aerogel waterborne coatings, building aerogel composites, cellulose-based structures, and aerogel-containing polymer films demonstrate several routes to combined optical and thermal functionality [14–17]. Microbead-filled coatings provide another structural route [18]. Barium sulfate is considered here as the solar-scattering phase, consistent with recent studies of fluorine-free particle modification and cellulose–barium sulfate coatings [19,20]. Its concentration in the reflective formulation is held constant. Thickness allocation, rather than repeated optimization of filler chemistry, is the principal independent variable. This restriction makes the comparison design interpretable and limits the number of interacting formulation factors.

The competition of interest is between optical saturation and loss of basecoat thermal resistance. Increasing topcoat thickness initially reduces solar absorption; after opacity develops, further thickening can displace insulating material with little additional solar rejection. We test whether the resulting minimum persists under alternative optical curves, jointly varied material, and boundary inputs, and a distributed coating-storage model. A second question is whether layer order remains influential when exposed optical properties

are held equal. The proposed evaluation framework integrates optical characteristics, thermal resistance, and transient heat-transfer behavior to systematically investigate the influence of layer thickness allocation on roof thermal performance. The findings provide a quantitative basis for understanding the coupled reflective–insulating mechanisms and offer useful guidance for the structural design and performance optimization of bilayer waterborne acrylic coatings.

2. Research Design, Materials and Methods

2.1. Study Boundaries and Hypotheses

Three interrelated mechanisms are examined: solar absorption exhibits diminishing returns with increasing reflective-layer thickness; retaining basecoat after optical saturation can reduce inward heat gain relative to a same-thickness reflector-only coating; and, under the specified elastic-property conditions, replacing the compliant basecoat with reflective material increases stored mismatch energy. The study examines the sensitivity of thermal response and elastic-energy estimates to the selected input parameters. These results clarify how material properties influence the preferred thickness allocation while distinguishing elastic energy storage from interfacial adhesion.

Figure 1 separates the optical boundary from the conductive pathway. A horizontal concrete slab carries a spatially uniform coating, with effective hemispherical irradiance applied at its exposed surface. The system contains no phase-change additive, active cooling device, or metallic infrared reflector. Lateral heat flow, precipitation, moisture transport, and mechanical damage are addressed separately through sensitivity analyses and the measurement framework. The reflective and insulating layer thicknesses are L_1 and L_2, respectively. Figure 1 was prepared using processed experimental photographs of the coated concrete specimen, with additional annotations to illustrate the bilayer structure and the associated heat-transfer pathways.

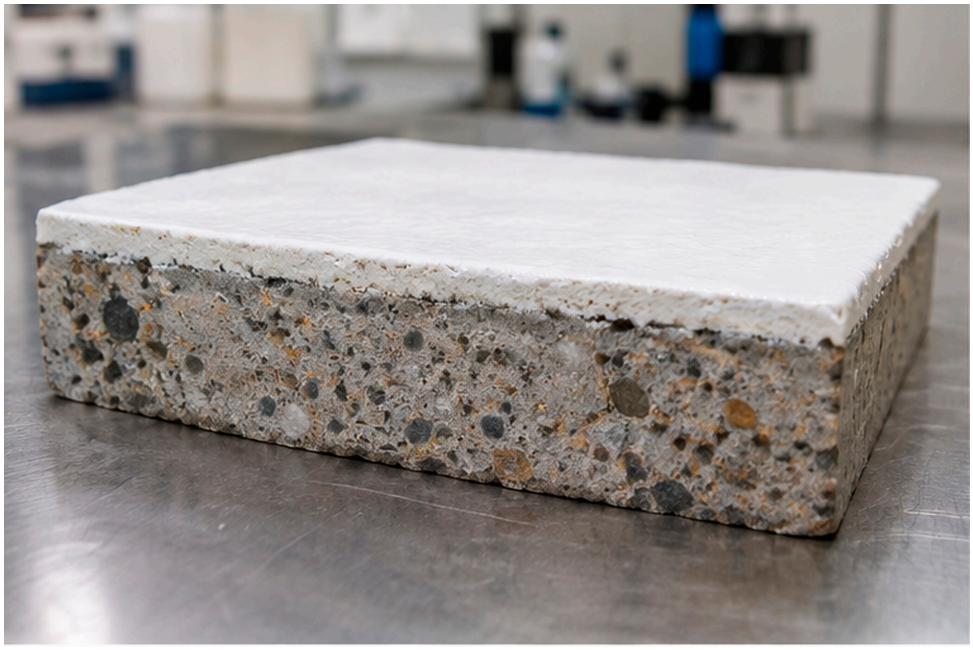


Figure 1. Bilayer coating architecture and design variables.

2.2. Candidate Formulations and Specimen Preparation

Table 1 gives formulation specifications and reference properties. The reflective formulation contains 55% barium sulfate and 45% acrylic binder on a dry-constituent volume basis; the

basecoat contains 45% aerogel granules and 55% binder by envelope volume. Aerogel envelope volume includes internal pores and differs from skeletal silica volume. Formulation stability, dispersant demand, rheology, shrinkage, and void formation are considered in the formulation-control procedure. Batch preparation requires density and solids-content measurements to convert the specified dry-volume fractions into wet-batch quantities.

Table 1. Dry formulation specifications and reference layer properties.

Quantity	Reflective Topcoat	Insulating Basecoat
Binder	Waterborne acrylic	Waterborne acrylic
Functional filler	Barium sulfate	Hydrophobic silica aerogel
Dry filler volume fraction	0.55	0.45
Dry binder volume fraction	0.45	0.55
Conductivity (W m^{-1} K^{-1})	0.300	0.075
Young's modulus (MPa)	350	60
Poisson ratio	0.35	0.30
Expansion coefficient (10^{-6} K^{-1})	60	35

The reflective phase uses a broad submicrometer-to-micrometer particle-size distribution, while the insulating phase uses aerogel granules substantially smaller than the thinnest applied basecoat. Particle-size distributions are included among the key material-characterization parameters. A higher-shear dispersion stage is appropriate for barium sulfate, whereas a lower-shear aerogel incorporation stage helps limit granule damage and binder penetration. Water and rheology modifiers are controlled to obtain a suitable application consistency, with additions documented on a mass basis. Porous polymer coatings and durable photonic coatings demonstrate why process-induced morphology can be as influential as the nominal recipe [21,22].

Achieving a coherent 2 mm dry coating requires coordinated control of the formulation, application, and curing conditions. High filler loading can raise viscosity, obstruct leveling, and create a binder-deficient film; rapid drying can add shrinkage stress and through-thickness cracks. Multiple thin passes, dispersion checks, and a measured intercoat interval provide key process controls for thermal characterization. Aerogel granule breakage or binder penetration can raise density and conductivity, while water uptake can persist despite a high surface contact angle. The incorporation of silica aerogel influences the internal pore structure and thermal conductivity of acrylic-based insulating coatings. Preserving aerogel porosity, limiting moisture absorption, and maintaining adequate cohesive strength are essential for achieving stable coating performance. Accordingly, the formulation design and curing procedure emphasize the coordinated control of material composition, microstructural integrity, and thermal properties to improve the overall performance of the bilayer coating system.

Figure 2 illustrates the specimen preparation and conditioning procedure. Figure 2 presents the specimen preparation and conditioning procedures using processed experimental photographs, illustrating the main stages of substrate preparation, insulating basecoat application, reflective topcoat application, and final conditioning. The concrete substrates were initially conditioned and thoroughly cleaned to remove surface contaminants and loose particles. The insulating basecoat was subsequently applied in successive controlled passes to achieve the designated dry-film thickness. After an intercoat interval of approximately 24 h, the reflective topcoat was applied, with its solid composition maintained consistently across all experimental groups. The prepared specimens were conditioned at 23 ± 2 °C and a relative humidity of 50% ± 5% for at least seven days until their masses stabilized. The compatibility between successive coating layers was assessed during the application process. Specimen mass, coated area, ambient conditions, and coating thickness were

recorded after each application pass. The positions of the specimens on the conditioning racks were randomized to minimize potential environmental variability.



Figure 2. Specimen preparation and conditioning sequence.

2.3. Thickness Allocation and Comparison Groups

The reflective fraction x is dry topcoat thickness divided by total dry coating thickness. Twelve allocations, including both single-layer endpoints, are evaluated at 2.0 mm total thickness. For a bilayer, the thickness ratio is $x/(1-x)$; $x = 0.35$ therefore corresponds to 0.70:1.30, or approximately 0.538:1. The bounded fraction accommodates the endpoints in plots. Table 2 defines the thickness-allocation matrix, with independent batches and specimens organized within each batch. Cross-sectional microscopy provides a means of determining local thickness distributions; these measurements are the appropriate inputs for specimen-level thermal assessments.

Four references distinguish mechanisms. Bare concrete measures the overall change caused by adding a reflective finish. The generic white-acrylic comparator is a 2.0 mm white-pigmented acrylic reference film, assigned reflectance 0.80, emissivity 0.92, and conductivity 0.20 W m^{-1} K^{-1}; these values define its effective optical and thermal properties. It is not the 55 vol% $BaSO_4$ reflector-only formulation. Homogeneous and reversed controls retain the nominal bilayer inventories and total thickness but change arrangement. The reflector-only endpoint matches total thickness while changing composition. Additional equal-optics controls isolate conductive effects under matched optical boundary conditions.

Equal thickness does not imply equal mass because the formulations differ in bulk density. Paired bilayer, mixed, and reversed specimens are compared on an equal-dry-inventory basis, with differences in constituent quantities documented. An areal balance links wet mass, solids fraction, and final dry mass. These records also support cost and environmental assessment; low density and a waterborne binder should be considered alongside manufacturing requirements in life-cycle evaluation.

Table 2. Specimen allocation matrix at 2.0 mm total dry coating thickness.

ID	Fraction x	Reflector (mm)	Basecoat (mm)
B000	0.00	0.00	2.00
B005	0.05	0.10	1.90
B010	0.10	0.20	1.80
B015	0.15	0.30	1.70
B020	0.20	0.40	1.60
B025	0.25	0.50	1.50
B030	0.30	0.60	1.40
B035	0.35	0.70	1.30
B040	0.40	0.80	1.20
B050	0.50	1.00	1.00
B075	0.75	1.50	0.50
B100	1.00	2.00	0.00
REF-B	—	0	0
REF-W	—	2.00	0
M035	0.35	Mixed	Mixed
R035	0.35	0.70 below	1.30 above

2.4. Optical and Conductive Constitutive Relationships

Solar reflectance is represented by a first-order optical saturation relationship. If the remaining reflectance deficit is $D = \rho_\infty - \rho_s$, the relation $dD/dL_1 = -D/\ell$ with $\rho s(0) = \rho b$ gives Equation (1). This effective relationship summarizes the thickness dependence of solar reflectance while remaining distinct from spectral scattering formulations such as Beer–Lambert, Mie and Kubelka–Munk approaches. Spectral scattering, absorption, pores, and substrate reflection are collapsed into three effective parameters. The reference values $\rho b = 0.700$, $\rho\infty = 0.955$, and $\ell = 0.120$ mm are retained as disclosed screening inputs; they define the reference optical parameter set.

$$\rho_s(x) = \rho_\infty - (\rho_\infty - \rho_b)\, exp(-xd/\ell) \quad (1)$$

A quantitative optical comparator is available from Li et al. [23]: a 60 vol% $BaSO_4$/acrylic paint had solar reflectances of 0.958, 0.962, 0.968, and 0.981 at dry thicknesses of 0.200, 0.224, 0.280, and 0.400 mm. The acrylic was solvent processed using dimethylformamide, so these data serve as an external optical benchmark rather than direct material-property data for the 55 vol% waterborne formulation. In particular, the reference asymptote of 0.955 lies below the reported paint values; it represents the lower-reflectance reference case. Equation (1) was evaluated against the four published points using least-squares regression with ρb fixed at 0.700 to obtain an external optical comparator. The regression-derived relationship was then used to examine sensitivity to an alternative optical response, while the joint analysis explored a wider parameter range.

The reference conductivities are 0.300 W m^{-1} K^{-1} for the reflective layer and 0.075 W m^{-1} K^{-1} for the basecoat. Their resistances act in series with one common contact resistance of 0.0002 m^2 K W^{-1}. This lumped term represents coating–concrete contact; the ideal interlayer resistance is zero. It is applied once to every coated comparator, so a changed number or order of layers does not introduce a hidden contact advantage. Table 3 lists the reference inputs; the listed values define the resolution of the reference calculations.

$$R_{coat} = \frac{xd}{k_r} + \frac{(1-x)d}{k_b} + R_{contact} \quad (2)$$

Table 3. Assigned thermal, optical, and boundary parameters.

Parameter	Value	Unit/Interpretation
Total dry thickness d	0.002	m
Limiting reflectance ρ∞	0.955	Reference solar-weighted value
Basecoat reflectance ρb	0.700	Reference
Optical saturation length ℓ	0.120	mm; reference value
Broadband emissivity ε	0.940	All bilayer allocations
Contact resistance	0.0002	m^2 K W^{-1}; coated systems
Concrete thickness	0.100	m
Concrete conductivity	1.40	W m^{-1} K^{-1}
Concrete density	2300	kg m^{-3}
Concrete heat capacity	880	J kg^{-1} K^{-1}
Exterior/interior h	12/8	W m^{-2} K^{-1}
Indoor air temperature	26	°C
Air mean/amplitude	30/5	°C/K; maximum at 15:00
Peak irradiance	950	W m^{-2}; daylight 06:00–18:00
Air–sky difference	10	K; reference case
Additional insulation	0	m^2 K W^{-1}; sensitivity value 2.5
Bare/white reflectance	0.35/0.80	Reference comparator values
Bare/white emissivity	0.90/0.92	Reference comparator values

For cured aerogel-containing paint, Abdul Halim et al. [24] reported conductivities of 0.11–0.07 W m^{-1} K^{-1} in 1.3 ± 0.2 mm water-based vinyl-acrylic films with 20, 40, and 60 vol% rice-husk-derived aerogel. These findings provide a conductivity benchmark for examining the reference value of 0.075 W m^{-1} K^{-1} in the 45% aerogel-envelope formulation. Raoufi et al. reported up to a 46% conductivity reduction at 50 vol% hydrophobic aerogel and explicitly treated partial resin intrusion. Binder entering granules replaces low-conductivity pore space and changes the effective composite volume fractions; crushing, intergranular voids, and binder continuity also matter. The nominal basecoat value is consequently the lower-conductivity reference condition. The joint analysis spans 0.070–0.150 W m^{-1} K^{-1}; its upper end represents a reduced-porosity condition for assessing the sensitivity of thermal performance.

The original mixed control uses $k_{mix} = k_r^{x}\ k_b^{(1-x)}$ and $\rho_{mix} = \rho b + x(\rho\infty - \rho b)$. The reversed control uses $\rho_{rev} = \rho b + (\rho\infty - \rho b)\exp(-L_2/0.150\ mm)$, representing attenuation through an exposed basecoat. The physical motivation is dilution of reflective material and masking of a buried reflector, and the corresponding relationships are treated as effective comparison descriptions. To assess the role of multiple scattering and retained porosity, these comparisons are supplemented by controls with equal reflectance and emissivity. Surface modification can alter optics as well as wettability [25], so equal visual whiteness is not a sufficient control.

For the equal-optics comparisons, the two-phase conductivity limits are $k_H = \left[\frac{x}{k_r} + \frac{1-x}{k_b}\right]$, $[k_A = xk_r + (1-x)k_b]$. The geometric value lies between them but is included as an intermediate effective-property estimate. The fixed reflectance is the reference bilayer value at x = 0.35, and every system has ε = 0.94. A separate reflectance sweep checks how changes in exposed optics affect the mixed and reversed comparisons while leaving conductive resistance unchanged.

2.5. Thermal Loading, Heat Transfer, and Response Metrics

The thermal-loading and measurement arrangement is illustrated in Figure 3. Figure 3 illustrates the thermal-loading and measurement arrangement based on processed experimental photographs, with annotations identifying the principal components of the testing apparatus and the corresponding temperature and heat-flux measurement locations. A coated concrete panel separates an external irradiation environment from a controlled indoor-side chamber. Thermocouple measurement positions include the exposed coating surface, coating–substrate vicinity, and room-facing surface, and a calibrated

heat-flux sensor records inward transmission. Sensor positions are specified in the central region away from the insulated panel edges. A calibrated lamp exposure permits controlled optical loading, while outdoor long-wave sky exchange is evaluated separately. Outdoor measurements additionally require the accompanying atmospheric boundary conditions. This distinction is particularly relevant when interpreting radiative cooling under humid or tropical conditions [26]. The distinction between lamp irradiation and outdoor sky radiative exchange is maintained when interpreting subambient cooling behavior.

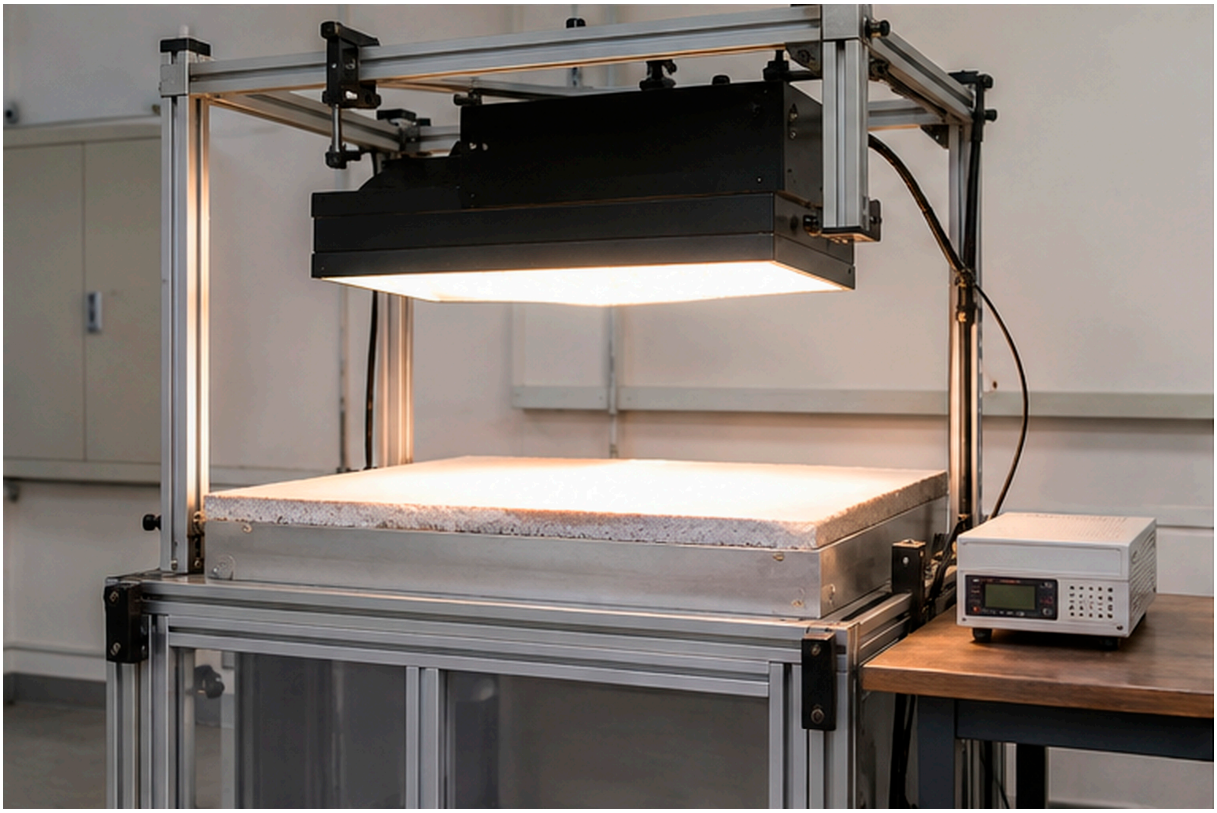


Figure 3. Thermal-loading arrangement and measurement locations.

Transient one-dimensional conduction is solved in a 100 mm concrete slab with constant conductivity, density, and heat capacity. Absorbed solar radiation is balanced by exterior convection, fourth-power long-wave exchange, and conduction into the assembly; indoor air remains at 26 °C. The principal heat-transfer formulation represents the coatings through their surface optical response and thermal resistance; a distributed-storage formulation is also evaluated to assess coating heat capacity. The reference roof is uninsulated; a comparison case adds 2.5 m^2 K W^{-1} at the indoor side without additional storage.

$$\rho_c c_c \frac{\partial T}{\partial t} = k_c \frac{\partial^2 T}{\partial z^2} \quad (3)$$

$$(1-\rho_s)G = h_o(T_s - T_a) + \varepsilon\sigma\left({T_{s,K}}^4 - {T_{sky,K}}^4\right) + q_{into} \quad (4)$$

The specified reference-day condition has a 950 W m^{-2} peak irradiance and half-sine daylight forcing from 06:00 to 18:00. Air temperature varies sinusoidally around 30 °C with a 5 K amplitude and peaks at 15:00; effective sky temperature is 10 K lower. Exterior and interior heat-transfer coefficients are 12 and 8 W m^{-2} K^{-1}. This reference-day forcing defines the boundary conditions for the comparative heat-transfer analysis. Humid-sky and cloudy cases are defined separately.

Signed daily heat transfer includes inward and outward fluxes, while positive inward heat gain integrates only room-directed flux and serves as the primary objective. The se-

lected metric quantifies roof-level heat transmission; conversion to electrical energy demand depends on building operation and equipment efficiency. Peak flux and timing characterize load concentration. With added insulation, the calculated room-facing temperature belongs to the complete assembly's interior surface, not the concrete underside.

$$q_{in} = h_i(T_{back} - T_{indoor}); Q_+ = \int_0^{24\ h} max(q_{in}, 0)\ dt \quad (5)$$

The concrete is discretized into N equal cell-centered control volumes, with N = 16 and $\Delta t = 60$ s in the main runs. For each cell, $C_i(T_i^{n+1} - T_i^n)/\Delta t$ equals the sum of end-of-step conductive fluxes, where $C_i = \rho c\ cc\ \Delta z$ per unit area. Interior conductance is $kc/\Delta z$. The first-cell conductance to the exterior surface is $[Rcoat + \Delta z/(2kc)]^{-1}$; the last-cell conductance to indoor air is $[1/hi + Rins + \Delta z/(2kc)]^{-1}$. The exterior surface has no storage. At each step, the coupled backward-Euler system is iterated using $hrad = \varepsilon\sigma(T_{s,K} + T_{sky,K})\ (T_{s,K}^2 + T_{sky,K}^2)$ until the surface-temperature change is below 10^{-9} K. The iteration cap is 12; the revised code flags failure rather than accepting an unconverged step. The batched implementation eliminates the same concrete system algebraically and is cross-checked against the archived solver.

All nodes begin at 26 °C. Seven identical 24 h forcing cycles are run, and only the seventh day is reported. Periodicity is checked afterwards from the slab start/end state and day-six/day-seven heat gains; it is not an adaptive stopping rule. The revised computations satisfy checks of 10^{-6} K in slab state and 10^{-6} Wh m^{-2} in successive daily heat gain. The energy residual integrates absorbed solar input minus radiation, convection, inward room flux, and the change in stored energy using the same end-of-step quadrature. The time integral in Equation (5) is divided by 3600 when time is in seconds so that Q^+ is reported in Wh m^{-2}; instantaneous q is reported in W m^{-2}.

To test omitted coating storage, a separate model retains four cells per nonzero coating layer and sixteen concrete cells, with the same total resistance and one coating–concrete contact term. Three reference topcoat/basecoat volumetric heat-capacity pairs, (1.5, 0.5), (2.0, 1.0), and (2.8, 1.5) MJ m^{-3} K^{-1}, define lower, nominal, and upper screening cases. The capacity pairs define a bounded material-property sensitivity assessment. Seven cycles and 60 s steps are used; a refined check uses eight cells per layer, sixty-four concrete cells, and 15 s steps. Nonlinear convergence is 10^{-10} K in this independent implementation. Section 3.7 reports both the effect on heat gain and the relevant capacity and diffusion scales.

Dark thermocouple adhesive can bias reflective-surface temperatures by increasing local absorption. Minimizing attachment area, documenting optical appearance, and independently checking selected readings are important temperature-measurement controls. Infrared thermography incorporates emissivity and reflected-surroundings corrections. Consistent heat-flux sensor mounting across groups reduces contact-resistance differences. Such biases matter when neighboring allocations differ only slightly.

2.6. Adhesion, Thermal Mismatch, and Conditioning Protocol

Figure 4 presents the pull-off loading arrangement and the relevant failure locations. Figure 4 presents the pull-off testing configuration and coating failure characteristics using processed experimental photographs, with annotations highlighting the loading arrangement, interlayer separation, cohesive basecoat fracture, and coating–concrete interfacial separation. The possible outcomes include interlayer separation, cohesive fracture within the aerogel-rich layer, and separation at the concrete interface.

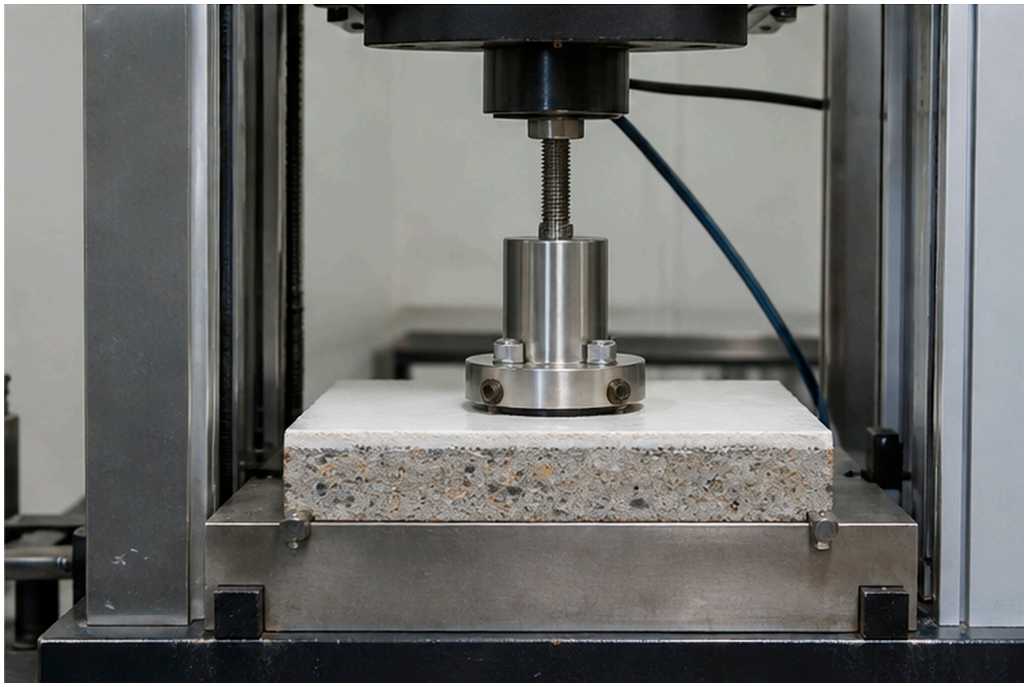


Figure 4. Pull-off test configuration and failure classifications.

Mechanical characterization records the peak force, bonded dolly area, loading history, and photographed failure surface with an unambiguous specimen identifier. Nominal pull-off stress is force divided by bonded area, but its interpretation depends on where the fracture occurs. A high nominal value accompanied by concrete failure gives a lower bound on coating adhesion; cohesive basecoat failure cannot automatically be described as poor topcoat adhesion. Failure-area fractions are evaluated consistently across the specimen groups.

Mechanical screening assumes fully restrained equibiaxial elasticity and a common 40 K temperature change. The reflective/basecoat moduli of 350/60 MPa, Poisson ratios of 0.35/0.30, and expansion coefficients of $60/35 \times 10^{-6}$ K^{-1} define the elastic-property reference case. Concrete is assigned 10×10^{-6} K^{-1}. For heating, expansion above that of the substrate produces compression; Equation (6) reports the magnitude. Cure shrinkage, humidity strains, relaxation, and local stress concentrations are treated as additional factors in interpreting the mechanical response.

$$|\sigma_j| = \frac{E_j \left|\alpha_j - \alpha_c\right| \left|\Delta T\right|}{1 - \nu_j} \tag{6}$$

$$U = \sum_j \frac{E_j}{1 - \nu_j} \left[\left(\alpha_j - \alpha_c\right)\Delta T\right]^2 d_j \tag{7}$$

Table 4 separates optical, conductive, and adhesion changes during conditioning. Independent specimens must be used for destructive adhesion tests and matched companions for optical and thermal characterization. The conditioning matrix includes 10–60 °C thermal cycles and 24 h water immersion. Their duration must reflect the intended environment and applicable procedures; exposure duration is interpreted on a cycle- and condition-specific basis.

Table 4. Characterization and conditioning program.

Measurement	Proposed Approach	Required Record
Thickness and morphology	Cross-sections at multiple locations	Actual layer thicknesses; original images
Solar reflectance	Integrating-sphere spectral measurement	Calibration, spectral range, weighting
Long-wave emissivity	Calibrated infrared characterization	Spectral or broadband definition
Conductivity	Several known dry thicknesses; contact correction	Temperature, density, repeatability
Thermal loading	Simultaneous reference panels; central sensors	Irradiance, air, sky, surface and heat flux
Pull-off adhesion	At least five locations per batch and condition	Dolly area, force history, failure fractions
Water exposure	24 h immersion screening; controlled redrying	Mass uptake and property retention
Thermal cycling	Indicative 10–60 °C; inspect at 0, 50, 100 cycles	Ramp, dwell, cracking and adhesion
Soiling/cleaning	Same deposit and cleaning sequence for controls	Reflectance before, after, and after cleaning

2.7. Parameter Sensitivity and Computational Verification Strategy

The eight ranges in Table 5 define a bounded joint-scenario analysis. A Latin-hypercube design generates 512 samples with uniform marginal coverage and seed 20261017. Every sample is evaluated at 39 fractions, x = 0.050, 0.075, ..., 1.000. Shared inputs, including total thickness, are identical within each bilayer/reflector-only pair. Uniform marginal coverage and independent sampling are used to explore the defined parameter domain. The ranges are informed by the optical and conductivity comparators but deliberately include poorer material performance. The resulting parameter bounds characterize the specified design and environmental sensitivity domain rather than statistical confidence intervals.

Table 5. Bounded inputs for the joint-scenario analysis.

Input	Range
Limiting reflectance $\rho\infty$	0.93–0.98
Basecoat reflectance ρb	0.65–0.75
Saturation length ℓ	0.060–0.200 mm
Topcoat conductivity kr	0.20–0.40 W m^{-1} K^{-1}
Basecoat conductivity kb	0.070–0.150 W m^{-1} K^{-1}
Long-wave emissivity ε	0.90–0.96
Exterior coefficient ho	8–20 W m^{-2} K^{-1}
Total dry thickness d	1.90–2.10 mm

The paired benefit is 100 $Q^+(1) - Q^+(x)Q^+(1)$. For each scenario, relative excess is $100[Q^+(x) - \min Q^+]/\min Q^+$, where the minimum is taken over by the sampled fraction grid. Scenario quantiles and counts summarize the influence of jointly varying design inputs on the preferred allocation. A separate manufacturing screen varies, d = 1.9, 2.0, and 2.1 mm and x near 0.35, while retaining reference properties. The fine allocation check uses x = 0.250–0.450 at 0.005 increments on four space/time grids (8 cells/120 s to 64 cells/15 s). The original twelve-candidate ranking is retained for direct comparison with the submitted calculation.

3. Results and Discussion

3.1. Optical Saturation and Conductive Resistance

Figure 5 contrasts the reference optical law with a regression-based relationship derived from published comparator data; Table 6 gives the original thickness-series properties. Under the reference law, reflectance is 0.7000, 0.9068, 0.9459, and 0.9543 at x = 0, 0.10, 0.20, and 0.35, respectively. These values represent the response of the specified optical relationship. Meanwhile, the series resistance decreases linearly as reflective material displaces basecoat.

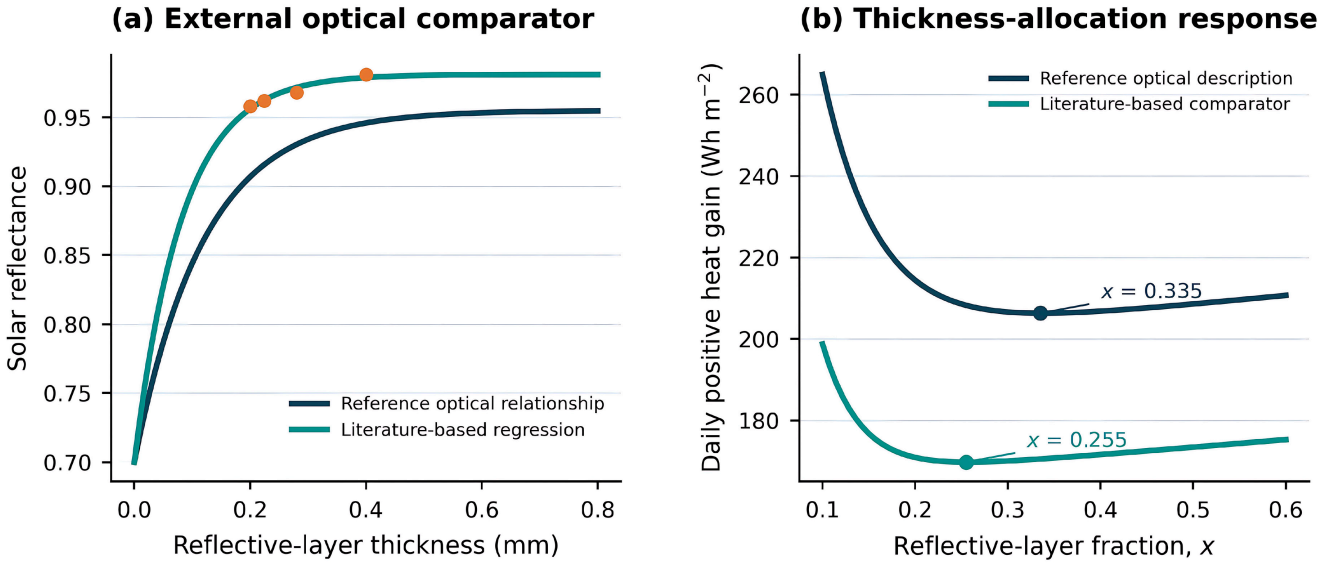


Figure 5. Influence of optical relationships on layer thickness allocation. (**a**) Reference and literature-based reflectance curves. (**b**) Daily inward heat gain under two optical descriptions.

Table 6. Calculated optical and conductive properties of the original thickness series.

Fraction x	Topcoat (mm)	Basecoat (mm)	Reflectance	Rcoat (m^2 K W^{-1})
0.00	0.00	2.00	0.7000	0.02687
0.05	0.10	1.90	0.8442	0.02587
0.10	0.20	1.80	0.9068	0.02487
0.15	0.30	1.70	0.9341	0.02387
0.20	0.40	1.60	0.9459	0.02287
0.25	0.50	1.50	0.9510	0.02187
0.30	0.60	1.40	0.9533	0.02087
0.35	0.70	1.30	0.9543	0.01987
0.40	0.80	1.20	0.9547	0.01887
0.50	1.00	1.00	0.9549	0.01687
0.75	1.50	0.50	0.9550	0.01187
1.00	2.00	0.00	0.9550	0.00687

At x = 0.35, coating resistance including contact is 0.01987 m^2 K W^{-1}, compared with 0.00687 m^2 K W^{-1} for reflector only. The approximately 0.013 m^2 K W^{-1} increment can affect an uninsulated roof after optical saturation but is modest relative to conventional insulation. Material conductivity and assembly resistance must therefore be interpreted together with thickness.

The external optical regression gives $\rho\infty$ = 0.98104 and ℓ = 0.08253 mm with a reflectance RMSE of 0.00231 against the four rounded literature values. When this optical relationship replaces the reference saturation description, the minimum shifts to x = 0.255

and $Q^+ = 169.76$ Wh m^{-2}; x = 0.35 gives 170.77 Wh m^{-2}. The shift is larger than the original allocation interval. Because the comparator differs in filler loading, solvent processing, and substrate, this shift illustrates the influence of optical characteristics on the selected layer-thickness fraction.

3.2. Transient Roof Response and Thickness Design Window

Figures 6 and 7 present the specified environmental forcing and calculated roof histories. Maximum exterior temperatures are 52.27 °C for bare concrete, 36.55 °C for white acrylic, and 31.33 °C for the selected bilayer. The temperature values characterize the highly reflective surface which can remain below ambient temperature when long-wave radiative losses offset absorbed radiation and convective heat input.

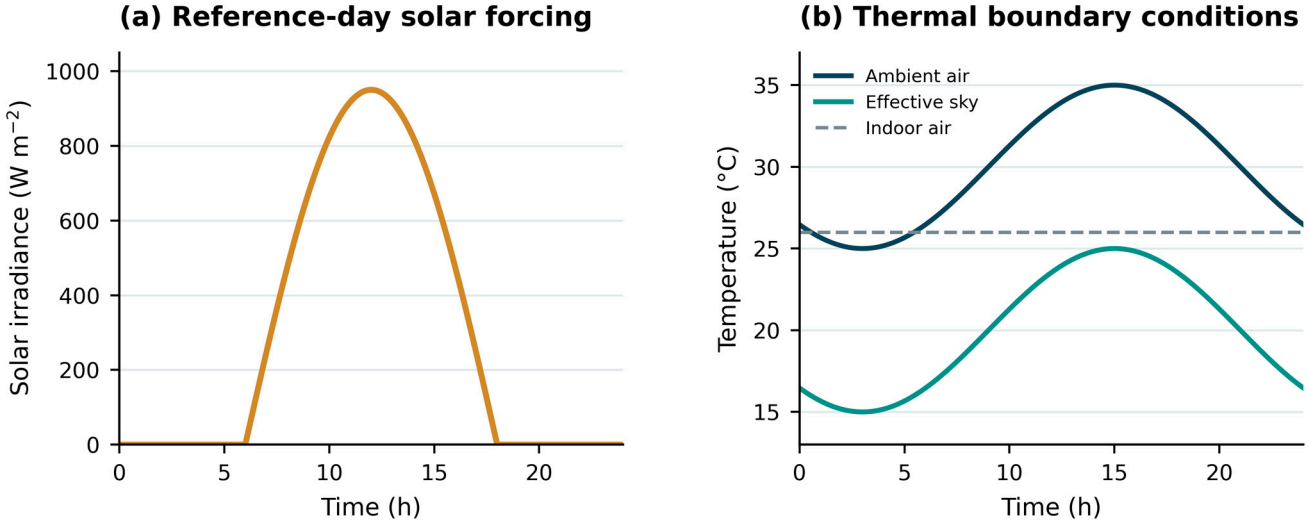


Figure 6. Reference-day boundary conditions. (**a**) Prescribed solar irradiance. (**b**) Air, effective sky, and controlled indoor temperatures.

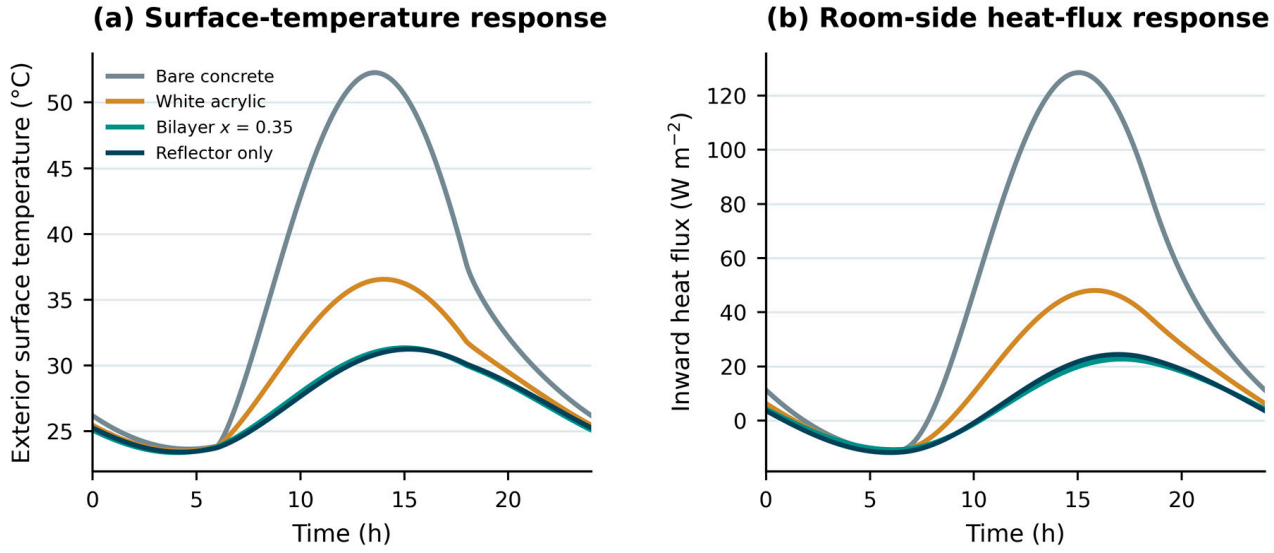


Figure 7. Calculated final-day thermal response of four reference systems. (**a**) Exterior surface temperature. (**b**) Room-side inward heat flux, with positive values directed toward the conditioned space.

Concrete storage delays inward flux relative to irradiance. The bilayer reaches 22.72 W m^{-2} at approximately 17:08, versus 24.41 W m^{-2} for reflector only; its maximum

interior temperature is 28.84 °C. Reflector only has a slightly lower maximum exterior temperature, 31.23 °C versus 31.33 °C, yet a higher inward heat gain. Surface-temperature minimization therefore does not necessarily minimize room-side heat transmission.

Table 7 gives a reduction from 1169.67 to 206.34 Wh m^{-2}, or 82.36%, relative to bare concrete under the reference inputs. The corresponding reduction against the same-thickness reflector-only coating is 6.11%, or 13.42 Wh m^{-2}. The larger bare-roof percentage principally reflects the changed optical boundary. The smaller paired comparison evaluates the basecoat after strong reflection has already been prescribed; its magnitude is governed by the specified conductivity and surface optical properties.

Table 7. Calculated final-day performance under the reference inputs.

System	Q^+ (Wh m^{-2})	Qnet (Wh m^{-2})	Peak q (W m^{-2})	Peak T_s (°C)	Peak Tb (°C)
Bare concrete	1169.67	1124.83	128.44	52.27	42.06
White acrylic	444.79	390.40	48.04	36.55	32.01
Basecoat only	546.24	504.58	58.02	40.31	33.25
Bilayer x = 0.35	206.34	142.47	22.72	31.33	28.84
Reflector only	219.76	148.48	24.41	31.23	29.05
Mixed control	443.04	391.45	47.66	36.95	31.96
Reversed control	562.98	517.61	60.29	40.17	33.54

Q^+ is positive inward heat gain and Qnet includes both flow directions; temperatures are separate trajectory maxima. White acrylic denotes a white-pigmented acrylic reference coating with a dry thickness of 2.0 mm, k = 0.20 W m^{-1} K^{-1}, ρs = 0.80, and ε = 0.92; these properties are specified for comparison.

It is distinct from the reflector-only 55 vol% $BaSO_4$/acrylic endpoint, which is also 2.0 mm thick. The white-acrylic reference provides a consistent conventional-coating benchmark for the analysis.

Signed daily heat transfer for the selected bilayer is 142.47 Wh m^{-2}, below its positive-only value because some nighttime heat flow is directed outward. This difference should remain visible in any energy interpretation. Discarding outward flux is appropriate for the chosen cooling-oriented screening metric, and is complemented by a full annual heat balance when translating results to whole-building energy performance. Climate-adaptive aerogel materials, tropical roof strategies, and analyses of complete roof systems all emphasize that the surrounding construction and climate affect applicability [27–29]. These findings identify how the thermal response varies with roof configuration and climate, thereby informing subsequent annual energy and indoor-comfort assessments.

Separate daily temperature maxima need not occur simultaneously. A maximum cooling difference requires synchronized paired readings and an identified time; the same applies to flux peaks. Peak delay may affect operating loads, but its value depends on the building schedule. No additional energy credit is assigned to delayed transmission here.

Figure 8 illustrates the effects of the reflective-layer thickness fraction on daily positive inward heat gain and peak inward heat flux under the reference conditions. Among the original twelve allocations, x = 0.35 gives the lowest positive heat gain. Fractions 0.30 and 0.40 give 206.61 and 206.82 Wh m^{-2}, only 0.13% and 0.23% higher. Refining the fraction spacing to 0.005 locates the reference minimum at x = 0.335, with Q^+ = 206.313 Wh m^{-2}, only 0.027 Wh m^{-2} below the x = 0.35 result. Thus, x = 0.35 is the best-performing point in the original candidate set, while x = 0.335 is the minimum on the refined reference grid. The 0.30–0.40 interval describes the shallow reference curve; the joint analysis in Section 3.6 tests whether it remains useful when inputs vary.

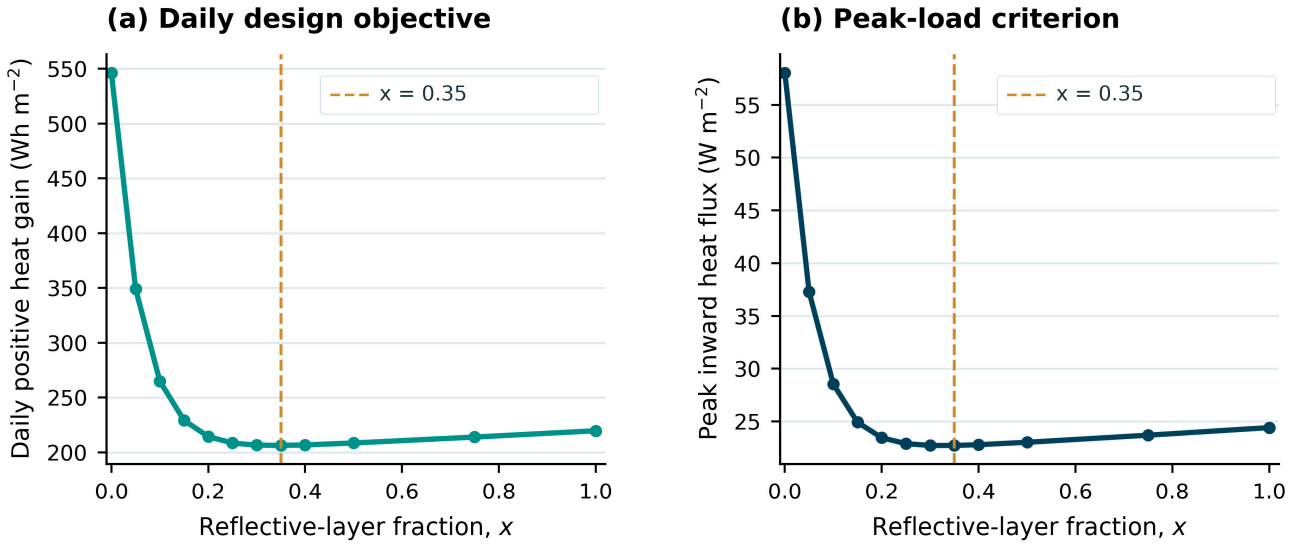


Figure 8. Thermal performance under different layer thickness ratios. (**a**) Daily heat gain. (**b**) Peak heat flux. The dashed line indicates x = 0.35; the refined minimum occurs at x = 0.335.

The minimum reflects competing marginal effects: absorbed solar input decreases exponentially under Equation (1), whereas the loss of conductive resistance per unit increase in x is constant under Equation (2). The competing trends explain the shallow optimum and identify saturation length and limiting reflectance as important characterization quantities for determining the practical design range.

Near-equivalent thermal allocations should be compared for coverage, basecoat protection, adhesion, and durability. Thicker topcoats may improve coverage but increase drying time, material use, and mismatch energy. Combining measured coverage, adhesion and durability constraints with the thermal response provide a practical basis for choosing among nearly equivalent allocations.

3.3. Architecture Controls and Mechanism Attribution

Under the original optical comparison relationships, the homogeneous and reversed controls give 443.04 and 562.98 Wh m^{-2}, respectively (Table 7). Their lower assigned reflectances account for most of this difference from the reference bilayer. Figure 9 and Table 8 therefore introduce a second comparison with reflectance fixed at 0.954253, emissivity at 0.94, and the same total thickness and contact resistance for all systems. The bilayer and reversed bilayer then give exactly the same heat gain, 206.34 Wh m^{-2}. This comparison shows that layer reversal does not change heat gain in the one-dimensional resistance formulation when the optical boundary and total resistance are matched.

For the homogeneous control, the ideal two-phase harmonic and arithmetic conductivity bounds are 0.10169 and 0.15375 W m^{-1} K^{-1}; the geometric interpolation gives 0.12184 W m^{-1} K^{-1}; with common optics, their heat gains are 206.34, 213.53, and 209.79 Wh m^{-2}, respectively. These bounds assume the same effective phases without extra interface resistance or changes in porosity. Actual mixing can change the phases themselves through infiltration or damage. A mixed control assigned reflectance 0.97 and geometric conductivity gives 188.42 Wh m^{-2}, below the nominal bilayer; at reflectance 0.90 it gives 285.28 Wh m^{-2}. Accordingly, matched optical characterization is essential for attributing performance differences to the bilayer architecture rather than to reflectance changes.

Effective conductivity is defined through the total material thickness, excluding the shared contact resistance. Harmonic and arithmetic limits assume unchanged effective

phases with no extra interface resistance; the geometric interpolation is used as an intermediate reference relationship.

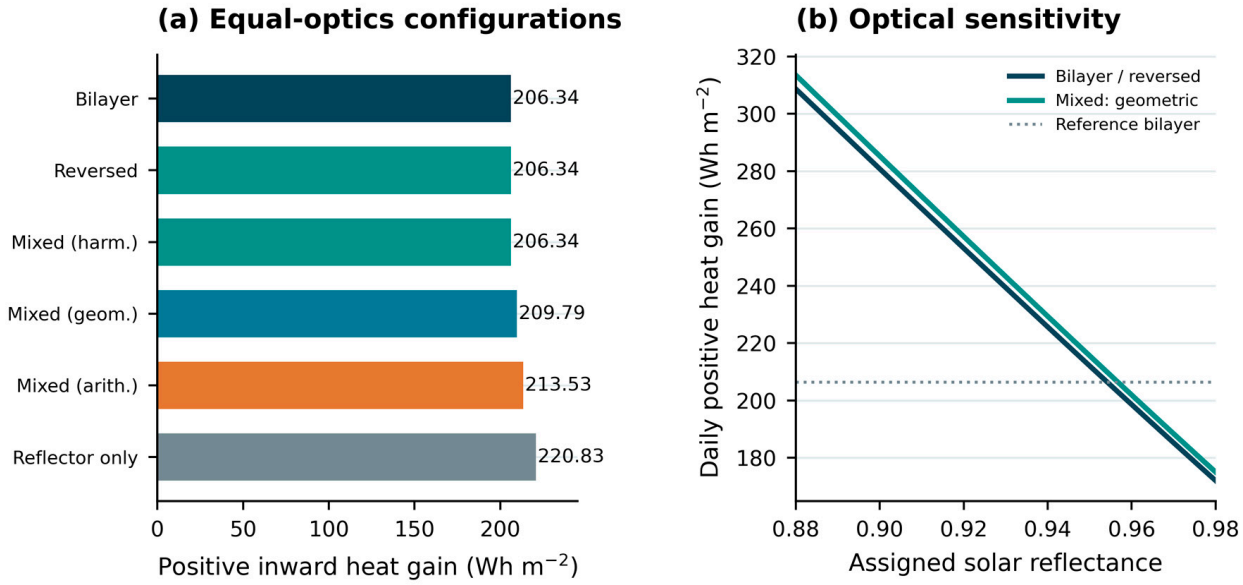


Figure 9. Effects of optical and conductive properties on coating thermal performance. (**a**) Inward heat gain under identical optical conditions. (**b**) Effect of solar reflectance on inward heat gain.

Table 8. Conductive comparison at equal reflectance (0.954253), emissivity (0.94), and total thickness (2.0 mm).

Configuration	Effective k ($W\ m^{-1}\ K^{-1}$)	Rcoat ($m^2\ K\ W^{-1}$)	Q^+ ($Wh\ m^{-2}$)
Bilayer x = 0.35	0.10169	0.01987	206.34
Reversed bilayer	0.10169	0.01987	206.34
Mixed harmonic bound	0.10169	0.01987	206.34
Mixed geometric interpolation	0.12184	0.01662	209.79
Mixed arithmetic bound	0.15375	0.01321	213.53
Reflector only at equal optics	0.30000	0.00687	220.83

Recent coating studies combine surface cooling with waste-derived constituents, polymer reinforcement, or other functions [30–32]. Such approaches broaden the design space, but they also add variables that can make causal interpretation difficult. The present study intentionally holds the two constituent formulations fixed. A future extension could compare different barium sulfate size distributions or aerogel surface treatments after the allocation mechanism is established. Adding several new fillers at the same time would require a different experimental design and substantially more controls. For thickness-allocation design, reproducible layer properties, confirmed layer geometry and comparison with independent roof-panel measurements provide the most informative evaluation criteria.

3.4. Mechanical Compatibility and Failure Interpretation

Figure 10 gives nominal restrained stress magnitudes of 1.08 MPa for the reflective layer and 0.086 MPa for the basecoat under a 40 K excursion. These values follow directly from the specified moduli and thermal-expansion mismatch. Under uniform restraint, the stress magnitude is independent of thickness. Both stress and stored energy scale linearly with $E/(1-\nu)$; multiplying both layer moduli by 0.5 or 2 multiplies both outputs by the same factors. The modulus values are considered independently of pull-off adhesion strength.

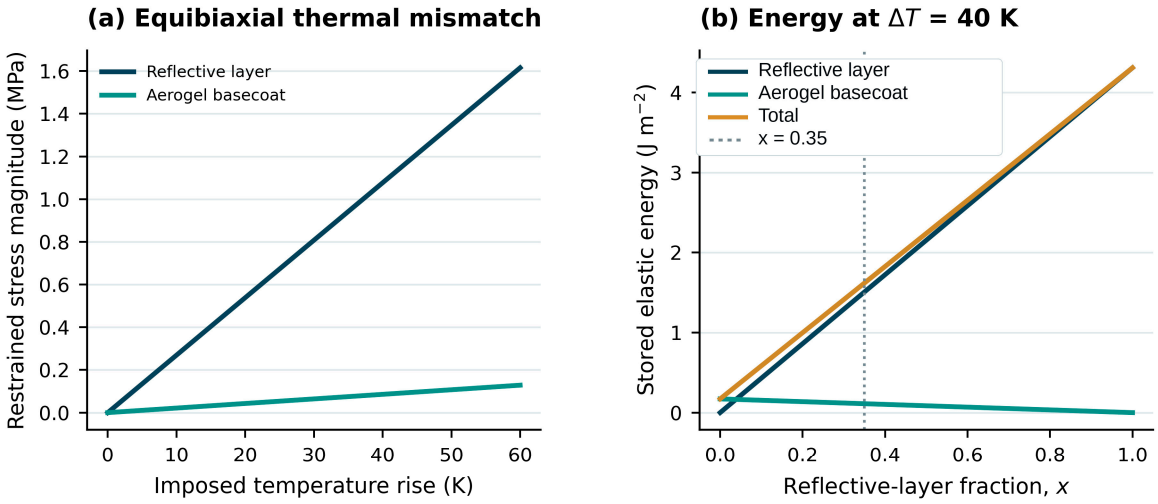


Figure 10. Equibiaxial elastic-response analysis. (**a**) Restrained stress magnitude versus imposed temperature change. (**b**) Stored elastic energy versus thickness allocation for a 40 K excursion.

At x = 0.35, the nominal stored energy is 1.62 J m^{-2}, compared with 4.31 J m^{-2} for reflector only. A common modulus multiplier of 0.5–2 changes the former to 0.81–3.24 J m^{-2}. Doubling the expansion mismatch or temperature excursion doubles stress but quadruples energy. If the relative layer moduli change independently, even the slope with allocation may change. Stored elastic energy is not the interfacial energy-release rate G for a specified crack and cannot be compared directly with adhesion strength. A fracture assessment would require geometry-dependent G, measured interfacial toughness, cure and moisture residual stresses, and a time- and temperature-dependent polymer constitutive law. Studies of concrete thermal cracking and aerogel interfaces [33,34] motivate such measurements and provide context for extending the present mechanical assessment.

The failure-assessment protocol includes full specimen photographs before and after loading, with scale bars and sample identifiers. For each fractured area, investigators should distinguish cohesive damage in the porous basecoat from separation at either interface. An increase in apparent pull-off stress accompanied by a shift into concrete failure is qualitatively different from a change caused by reduced porosity in the basecoat. Coupled thermal insulation and protective coatings can involve similarly competing functions on other substrates [35]. For concrete roofs, mechanical acceptance must be established on the intended substrate and after relevant conditioning. The failure schematics distinguish fracture locations and support interpretation of subsequent pull-off observations.

3.5. Environmental Sensitivity and Roof-Assembly Dependence

Table 9 and Figure 11 evaluate environmental and material perturbations at x = 0.35. A warmer effective sky increases inward gain. Higher exterior convection also raises gain while the reflective surface is cooler than ambient; convection would cool a hotter absorbing surface. Under the prescribed cloudy scenario, reduced long-wave cooling outweighs part of the reduced solar input, so positive gain can exceed the clear-day value.

Increasing basecoat conductivity from 0.075 to 0.135 W m^{-1} K^{-1} reduces the advantage over reflector only from 6.11% to 2.30%. This conductivity variation represents the influence of possible changes in retained aerogel porosity. Reducing both endpoint reflectances by 0.06 raises bilayer gain to 288.82 Wh m^{-2}. A loss of 0.01 raises it to approximately 219.89 Wh m^{-2}, slightly above the reference reflector-only coating at 219.76 Wh m^{-2}. Comparisons must therefore match aging and cleaning conditions.

Table 9. Calculated condition comparison at fixed x = 0.35.

Scenario	Changed Condition	Bilayer Q^+ ($Wh\ m^{-2}$)	Reflector Q^+ ($Wh\ m^{-2}$)	Reduction (%)
Reference	Reference inputs	206.34	219.76	6.11
Humid sky	Air–sky difference 3 K	344.07	362.72	5.14
Windy	Exterior h = 25 $W\ m^{-2}\ K^{-1}$	289.32	308.98	6.36
Hot day	Air mean 35 °C	573.90	601.61	4.60
Cloudy	Gmax = 450 $W\ m^{-2}$; sky gap 3 K	309.00	326.46	5.35
Wet base	Basecoat k = 0.135 $W\ m^{-1}\ K^{-1}$	214.70	219.76	2.30
Reflectance loss	Both reflectance endpoints −0.06	288.82	306.82	5.87
Insulated roof	Added indoor-side R = 2.5 $m^2\ K\ W^{-1}$	17.35	18.03	3.80

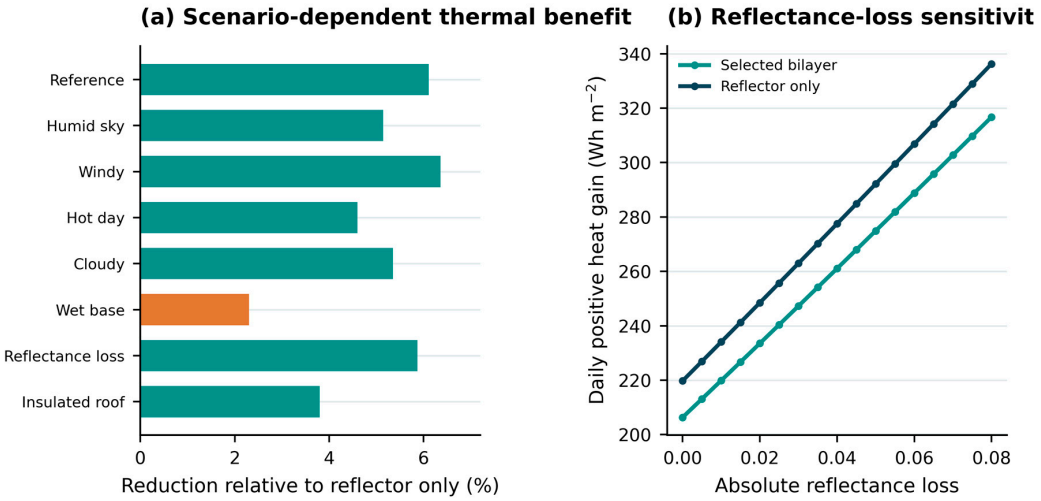


Figure 11. Sensitivity of roof heat gain to environmental and material conditions. (**a**) Reduction relative to the reflector-only reference. he orange bar highlights the wet-base scenario with increased basecoat thermal conductivity (0.135 $W\ m^{-1}\ K^{-1}$). (**b**) Effect of solar reflectance loss.

With added indoor-side insulation of 2.5 $m^2\ K\ W^{-1}$, the bilayer and reflector-only heat gains are 17.35 and 18.03 $Wh\ m^{-2}$, respectively: the absolute difference is only 0.69 $Wh\ m^{-2}$, despite a 3.80% relative difference. The reference uninsulated difference of 13.42 $Wh\ m^{-2}$ corresponds to 0.56 $W\ m^{-2}$ when averaged over 24 h. The small absolute differences highlight the relevance of fabrication consistency and heat-flux measurement uncertainty. Whole-building energy implications further depend on annual climate, roof area, HVAC efficiency, and operating schedules. Phase-change coatings [36,37] and spectrally selective surfaces [38] represent additional mechanisms that would require their own constitutive treatment.

3.6. Joint Uncertainty Propagation and Manufacturing Tolerance

Figure 12 and Table 10 summarize the 512 paired bounded scenarios. Minimizing fractions on the 0.025 grid span 0.175–0.625, with 5th/50th/95th scenario percentiles of 0.225/0.375/0.575. Only 172 of the 512 minima lie in 0.30–0.40. For fixed x = 0.35, the paired percentage reduction relative to reflector only spans −3.74% to 7.43%, with 5th/50th/95th

percentiles of −1.00%/2.87%/6.07%; the reduction is negative in 51 scenarios. These results demonstrate that the preferred fraction and paired heat-gain reduction vary across the selected parameter ranges, supporting a design approach based on measured material properties and environmental conditions.

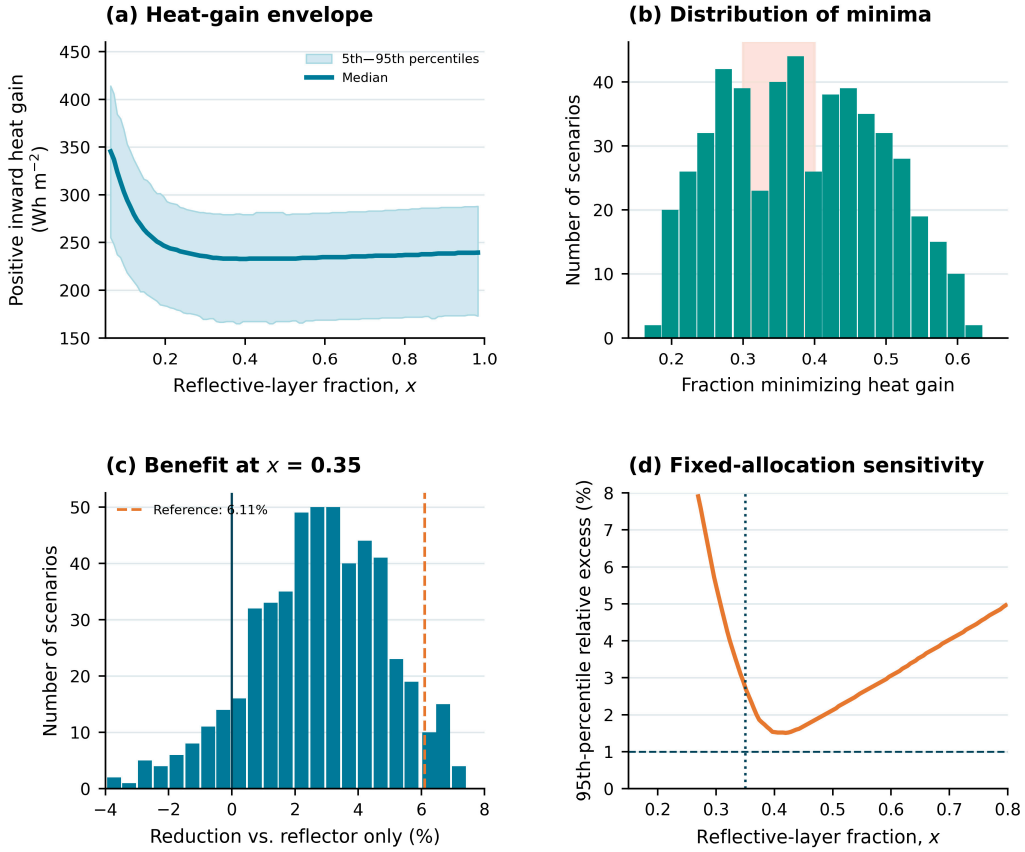


Figure 12. Sensitivity analysis of layer thickness allocation. (**a**) Heat-gain uncertainty range. (**b**) Distribution of optimal thickness fractions. (**c**) Heat-gain reduction at x = 0.35. (**d**) Relative excess heat gain.

Table 10. Conditional summaries across the 512 bounded joint scenarios.

Quantity	5th Percentile	Median	95th Percentile
Minimizing fraction x	0.225	0.375	0.575
Q^+ at x = 0.35 (Wh m^{-2})	165.77	233.05	281.24
Paired benefit (Wh m^{-2})	−2.16	6.84	15.48
Paired benefit (%)	−1.00	2.87	6.07
Relative excess at x = 0.35 (%)	0.00	0.37	2.81

At x = 0.35, the median relative excess above each scenario's best grid value is 0.37%, increasing to 2.81% at the 95th scenario percentile. No tested fixed fraction keeps that percentile below 1%; the smallest value is 1.49% at x = 0.425. The optimum therefore depends on the selected parameter domain and performance criterion. A separate manufacturing screen, holding material and climate inputs at their reference values while varying total thickness from 1.9 to 2.1 mm and x from 0.325 to 0.375, gives Q^+ = 204.93–207.87 Wh m^{-2}. This spread exceeds the difference between the original neighboring candidates. The thickness ranges provide a manufacturing-tolerance sensitivity assessment.

3.7. Numerical Verification and Coating-Storage Assessment

Table 11 shows that the fine-grid minimum remains at x = 0.335 through all four joint space/time refinements. At x = 0.35, changing from 16 cells/60 s to 64 cells/15 s increases Q^+ from 206.340 to 206.501 Wh m^{-2}, a 0.078% difference. The changes among neighboring fractions persist numerically, but are much smaller than the input-scenario variation. The batched and original solvers agree within 1.3×10^{-10} Wh m^{-2} at the four checked fractions. The joint-scenario final-day energy residual is below 6.9×10^{-7} J m^{-2}. These verification results establish strong numerical consistency for the defined heat-transfer equations and parameter conditions.

Table 11. Stability of the reference minimum under joint space/time refinement.

Cells/Δt (s)	Q^+ at x = 0.30	Q^+ at x = 0.35	Q^+ at x = 0.40	Minimizing x
8/120	206.319	206.052	206.530	0.335
16/60	206.606	206.340	206.819	0.335
32/30	206.718	206.453	206.932	0.335
64/15	206.766	206.501	206.981	0.335

The concrete areal heat capacity is 202,400 J m^{-2} K^{-1}. At x = 0.35, the nominal coating capacity is 2700 J m^{-2} K^{-1} (1.33% of concrete), increasing to 3910 J m^{-2} K^{-1} (1.93%) in the upper case. Characteristic diffusion times $L_i^2 C_{v,i}/k_i$ are 3.27 and 22.53 s for the nominal topcoat and basecoat; upper-case values are 4.57 and 33.80 s. The longest coating diffusion scale across the full allocation range is 80 s, compared with approximately 4.02 h in the concrete and a 24 h forcing period. These characteristic diffusion scales clarify the relative importance of coating and concrete heat storage.

Explicit reference coating storage gives Q^+ = 206.053 Wh m^{-2} at x = 0.35, 0.139% below the capacity-free value; the upper case gives 205.921 Wh m^{-2}, 0.203% lower. Its paired reflector-only value is 219.061 Wh m^{-2}, changing the benefit from 6.107% to 5.998%. All three capacity cases retain x = 0.35 as the lowest of the original twelve candidates. The refined upper-capacity model gives 206.082 and 219.233 Wh m^{-2}, again a 5.998% benefit. This supports the capacity-free approximation for the daily reference comparison within the tested envelope, while its correction is large enough to matter when interpreting the shallow minimum. Rapid irradiation transients or thicker films require a separate storage analysis.

3.8. Experimental Verification Framework and Applicability

Table 12 summarizes the material measurements and independent roof-panel tests needed to assess the optical and heat-transfer relationships. The validation protocol specifies at least three independently prepared panels per shortlisted system for controlled-rig testing followed by outdoor exposure. The protocol calls for randomized panel positions and concurrent exposure of bare and reflector-only references. The comparisons cover complete temperature and heat-flux histories, daily inward heat gain, and peak timing. Material-parameter calibration and independent validation are distinguished by specimen batch or exposure day. Layer thicknesses and surface optical properties should be recorded before each exposure to distinguish fabrication variability from changes caused by weather, moisture, or repeated conditioning of the specimens.

Table 12 defines quantitative targets for independent validation. The original 5% daily heat-gain bias target is approximately 10.3 Wh m^{-2} at the reference bilayer response, close to the 13.42 Wh m^{-2} paired benefit; meeting that target alone would not resolve the architecture effect. A constant inward-flux offset of 0.5 W m^{-2} can change the integrated positive heat gain by at most 12 Wh m^{-2} over 24 h, because the positive-part operation is 1-Lipschitz. Differences of 0.27–0.48 Wh m^{-2} between neighboring allocations require substantially

tighter paired uncertainty. The protocol must estimate sensor bias, mounting effects, batch variation, and thickness variability together. Independent preparation batches are retained as the primary basis for assessing repeatability.

Table 12. Experimental verification criteria.

Stage	Proposed Criterion	Evidence Required
Optical calibration	Reflectance regression residual ≤ 0.01 absolute	Independent thickness series and calibration record
Thickness control	Total thickness within $\pm 5\%$ of target	Measured cross-sections; actual values used in model
Conductivity calibration	Repeatability target $\leq 5\%$	Independent batches; contact-resistance correction
Controlled thermal validation	Temperature RMSE target ≤ 1 K	Held-out panels and synchronized temperature series
Heat-transfer validation	Initial daily Q^{+} bias target $\leq 5\%$; insufficient alone to resolve the paired benefit	Calibrated flux integration with uncertainty budget
Architecture detection	Resolve a 13.42 Wh m^{-2} reference difference	Pilot variance and justified sample size
Mechanical assessment	Application-specific adhesion gate to be set	Measured strengths, original failure photographs
Outdoor validation	No parameter re-adjustment on validation days	Concurrent controls, weather and sky-boundary data

Independent validation examines time-dependent residuals. Daytime temperature bias may indicate incorrect optics or convection; flux phase error may reflect substrate storage or sensor timing. Post-wetting disagreement may reveal conductivity changes. These factors are evaluated separately to preserve the physical interpretation of parameter changes. Residuals against time, irradiance, and air temperature help identify compensating model errors.

The framework links optical saturation, series resistance, and controlled validation to clarify the mechanisms governing thickness allocation. The adopted formulation uses effective grey-sky exchange, constant convection and one-dimensional conduction; moisture transport and polymer relaxation can be incorporated in extensions of the method. The main capacity-free calculation is supplemented by the coating-storage assessment in Section 3.7. Independent optical, thermal, and adhesion tests provide the basis for extending these results to specific coating formulations and service environments.

4. Conclusions

This integrated optical–thermal investigation examines thickness allocation in a water-borne acrylic coating with a barium sulfate reflective topcoat and a silica aerogel insulating basecoat. Total dry thickness is fixed at 2.0 mm, and roof-level heat transmission is evaluated separately from surface cooling. The results identify the sensitivity of thickness allocation to optical response, thermal resistance, and roof boundary conditions. The following conclusions can be drawn:

(1) Under the reference inputs, $x = 0.35$ is the lowest of the original twelve candidate fractions, giving 206.34 Wh m^{-2} daily positive inward heat gain. A 0.005 fraction grid places the minimum at $x = 0.335$ with only a 0.013% improvement. The refined grid

and space–time checks consistently locate this reference minimum, while the broader parameter study characterizes its dependence on material properties.

(2) The reference reduction of 6.11% relative to reflector only is 13.42 Wh m^{-2} in absolute terms. Across 512 bounded joint scenarios, the minimizing fraction spans 0.175–0.625 and the fixed-x = 0.35 benefit has 5th–95th scenario percentiles of −1.00% to 6.07%, with negative benefit in 51 cases. These findings favor selecting the thickness ratio on the basis of material characterization and the intended thermal boundary conditions.

(3) Reversing the layer order has no effect in the capacity-free one-dimensional model when surface optics and total series resistance are equal. The original mixed and reversed rankings depend strongly on their assigned reflectance values. Matched-inventory and equal-optics comparisons answer different questions and together provide a practical framework for subsequent physical comparisons.

(4) Distributed coating storage changes the reference paired benefit to approximately 6.00% within the specified heat-capacity range. This supports the daily-load approximation but is comparable to the small differences among neighboring candidates. The benefit falls to 0.69 Wh m^{-2} with conventional roof insulation. The elastic mismatch assessment also identifies stored-energy trends that can guide targeted adhesion and durability characterization.

(5) Numerical refinement and energy-balance checks support the internal consistency of the calculation. The resulting computational consistency provides a stable basis for independent laboratory and roof-panel validation. Beyond material calibration and panel testing, a useful extension is a climate-dependent annual model coupling spectral optics, moisture-dependent conductivity, and progressive soiling with measured coating damage and renewal schedules. Such a model could optimize service-period heat transfer and maintenance cost jointly, including the winter heating penalty, rather than selecting a fraction from a single clear day.

The results obtained in this study provide a useful reference for the thickness design of bilayer reflective–insulating coatings under the investigated conditions. However, the preferred thickness ratio and its associated thermal benefits may vary with material properties, coating preparation conditions, substrate characteristics, and environmental exposure. The practical applicability of the proposed configuration should therefore be considered in relation to the specific material system and service environment. Further material characterization and long-term performance assessment would help establish its suitability for broader engineering applications.

Author Contributions: Conceptualization, L.J., J.M., and J.X.; methodology, L.J. and J.M.; formal analysis, L.J.; investigation, J.M.; resources, L.J.; data curation, L.J.; writing—original draft preparation, J.X.; writing—review and editing, J.M.; visualization, J.M.; supervision, J.M.; project administration, L.J. All authors have read and agreed to the published version of the manuscript.

Funding: This research received no external funding.

Institutional Review Board Statement: Not applicable.

Informed Consent Statement: Not applicable.

Data Availability Statement: The datasets used during the current study are available from the corresponding author.

Acknowledgments: The authors thank the research group members for their guidance.

Conflicts of Interest: The authors declare no conflicts of interest.

References

1. Zhang, W.; Jiao, D.; Zhao, B.; Pei, G. Experimental and numerical investigation of the effects of passive radiative cooling-based cool roof on building energy consumption. *Appl. Energy* **2024**, *376*, 124161. [CrossRef]
2. Liu, J.; Xie, L.; Wu, H.; Zhang, G.; Fang, C.; Gu, J. Exploring energy-saving performance of radiative cooling roofs with a transient heat transfer model. *J. Build. Eng.* **2024**, *88*, 109174. [CrossRef]
3. Xuan, Q.; Lao, J.; Zhao, B.; Li, G.; Pei, G.; Niu, J.; Dai, J.-G. Experimental and numerical investigation on energy-saving performance of radiative cooling coating for metal container office. *Energy Build.* **2024**, *310*, 114084. [CrossRef]
4. De Masi, R.F.; Festa, V.; Ruggiero, S.; Russo, A.; Villano, F. Aging, soiling, and cleaning effects on cool roof performance: Experimental insights on aerogel-based and conventional reflective coatings in Mediterranean climate. *J. Build. Eng.* **2025**, *116*, 114577. [CrossRef]
5. Chen, Z.; Li, D.; Yao, S.; Duan, Y.; Chen, J.; Liu, M.; Liu, T.; Li, Z. Effects of Silica Aerogel Content on the Properties of Waterborne Organic Thermal Insulation Coatings. *Gels* **2025**, *11*, 547. [CrossRef] [PubMed]
6. Yu, Z.; Xu, J.; Zhu, N.; Cheng, J.; Lan, X.; Liao, J. Bilayer-Structured Passive Radiative Cooling Coating with Thin Thickness, Highly Scattering, and Enhanced Thermal Dissipation. *Langmuir* **2025**, *41*, 12365–12374. [CrossRef] [PubMed]
7. Wang, X.; Li, L.; Zhang, S.; Ren, D.; He, P.; Yang, S.; Han, R. Tailoring bilayer passive radiative cooling coating for sustainable building and vehicle thermal management. *Constr. Build. Mater.* **2026**, *518*, 145852. [CrossRef]
8. Nie, H.; Huang, L.-B.; Xu, X.; Li, Z.; Liu, H.; Wang, H.; Yang, C. Hierarchically Porous–Dense bilayer coating with improved solar reflection and outdoor durability for radiative cooling. *Compos. Commun.* **2026**, *62*, 102729. [CrossRef]
9. Song, X.; Liu, L.; Farooq, A.S.; Tso, C.Y.; Zhang, P. Simulated and experimental evaluation of optical property of the polymeric radiative cooling coating with gradient-dispersed particles. *Int. J. Therm. Sci.* **2025**, *213*, 109819. [CrossRef]
10. Raoufi, F.; Montazeri, S.; Rastegar, S.; Asadi, S.; Ranjbar, Z. Optimizing thermal insulation of waterborne acrylic coatings through controlled integration of hydrophobic silica aerogel: Experimental insights and advanced modeling. *J. Mater. Res. Technol.* **2025**, *38*, 5630–5638. [CrossRef]
11. Yao, B.; Yao, C.; Mao, X. Preparation of SiO_2 aerogel-based waterborne thermal insulation coatings with functionally graded structure. *Chin. J. Chem. Eng.* 2026, *in press*. [CrossRef]
12. Zhao, J.; Yang, B.; Chen, Z.; Zeng, Y. Preparation and Performance of Thermal Insulation Waterborne Polyurethane Coatings Containing 3-Aminopropyltriethoxysilane Modified Organo-Bridged Silica Aerogel. *Coatings* **2025**, *15*, 1021. [CrossRef]
13. Xiang, Y.; Yan, M.; Li, L.; Xiao, Y.; Sun, H.; Zhang, Z.; Yang, H.; Cheng, X.; Pan, Y. Low thermal conductivity and self-cleaning silica aerogel coating based on a secondary coating encapsulation strategy. *Constr. Build. Mater.* **2025**, *472*, 140878. Correction in *Constr. Build. Mater.* **2026**, *528*, 146490. [CrossRef]
14. Han, D.; Wang, C.; Han, C.B.; Cui, Y.; Ren, W.R.; Zhao, W.K.; Jiang, Q.; Yan, H. Highly Optically Selective and Thermally Insulating Porous Calcium Silicate Composite SiO2 Aerogel Coating for Daytime Radiative Cooling. *ACS Appl. Mater. Interfaces* **2024**, *16*, 9303–9312. [CrossRef] [PubMed]
15. He, S.; Li, H.; Zhang, Y.; Sheng, H.; Huang, Y. Silica aerogel composites with excellent thermal insulation for building applications. *Energy Build.* **2025**, *346*, 116169. [CrossRef]
16. Liu, Y.; Bu, X.; Liu, R.; Feng, M.; Zhang, Z.; Yuming, Z. Robust fluorinated cellulose composite aerogels incorporating radiative cooling and thermal insulation for regionally adaptable building thermal management. *Int. J. Biol. Macromol.* **2025**, *292*, 139239. [CrossRef] [PubMed]
17. Li, Y.; Zhang, X.; Zhang, T.; Chen, Y.; Zhang, S.; Yu, D.; Wang, W. Radiative cooling materials prepared by SiO_2 aerogel microspheres@PVDF-HFP nanofilm for building cooling and thermal insulation. *Ceram. Int.* **2024**, *50*, 48031–48040. [CrossRef]
18. Long, H.; Wang, F.; Zhao, Y.; Ou, J.; Li, W.; Amirfazli, A. Hollow ceramic microbeads-SiO_2/polydimethylsiloxane radiative cooling coating with self-cleaning effect and thermal insulation capability. *Prog. Org. Coat.* **2025**, *200*, 109075. [CrossRef]
19. Chen, G.; Zheng, Z.; Zhang, P. Fluorine-free super-hydrophobic barium sulfate particles for passive daytime radiative cooling. *Mater. Lett.* **2025**, *393*, 138560. [CrossRef]
20. Bijarniya, J.P.; Tripathi, S.; Bauri, S.; Sarkar, J.; Maiti, P. Hydrophobic self-sustained natural cellulose-$BaSO_4$ composite coating for efficient daytime radiative cooling. *Cellulose* **2025**, *32*, 2353–2365. [CrossRef]
21. Yan, Y.; Cui, P.; Wu, S.; Wei, H.; Zhong, S.; Sun, W. Dynamic fabrication of porous polymeric coating for efficient passive daytime radiative cooling using in-situ pore-formation strategy. *Polymer* **2024**, *307*, 127327. [CrossRef]
22. Xu, X.-Y.; Zhang, H.; Kang, X.-J.; Zhang, Y.-Z.; He, C.-Y.; Gao, X.-H. High-performance, superhydrophobic, durable photonic structure coating for efficient passive daytime radiative cooling. *Mater. Today Phys.* **2024**, *48*, 101556. [CrossRef]
23. Li, X.; Peoples, J.; Yao, P.; Ruan, X. Ultrawhite $BaSO_4$ Paints and Films for Remarkable Daytime Subambient Radiative Cooling. *ACS Appl. Mater. Interfaces* **2021**, *13*, 21733–21739. [CrossRef] [PubMed]
24. Halim, Z.A.A.; Ahmad, N.; Yajid, M.A.M. Modifying commercial water-based acrylic paint with Rice husk-derived silica aerogel fillers for building thermal insulation. *Prog. Org. Coat.* **2025**, *201*, 109114. [CrossRef]
25. Yang, N.; Liu, J.-H.; Kai, M.-F.; Dai, J.-G. Geopolymer-based radiative cooling coating: Tailoring surface hydrophobic properties while retaining optical characteristics. *Constr. Build. Mater.* **2024**, *428*, 136373. [CrossRef]

26. Mishra, B.R.; Sundaram, S.; Sasihithlu, K. Cooling Performance of TiO_2-Based Radiative Cooling Coating in Tropical Conditions. *ACS Omega* **2024**, *9*, 49494–49502. [CrossRef] [PubMed]
27. Liu, Y.; Bu, X.; Liu, R.; Feng, M.; Zhang, Z.; He, M.; Huang, J.; Zhou, Y. Construction of robust silica-hybridized cellulose aerogels integrating passive radiative cooling and thermal insulation for year-round building energy saving. *Chem. Eng. J.* **2024**, *481*, 148780. [CrossRef]
28. Khorat, S.; Das, D.; Khatun, R.; Aziz, S.M.; Anand, P.; Khan, A.; Santamouris, M.; Niyogi, D. Cool roof strategies for urban thermal resilience to extreme heatwaves in tropical cities. *Energy Build.* **2024**, *302*, 113751. [CrossRef]
29. Wang, Y.; Wang, Z.-H.; Rahmatollahi, N.; Hou, H. The impact of roof systems on cooling and building energy efficiency. *Appl. Energy* **2024**, *376*, 124339. [CrossRef]
30. Wang, M.; Tan, X.; Jin, L.; Qi, G.; Hu, W.; Chen, S.; Li, S.; Qiao, Y.; Chen, X.; Qiu, S. The Utilization of β-Hemihydrate Phosphogypsum Coating with Radiative Cooling and Superhydrophobic Properties for Outdoor Cooling Requirements. *Coatings* **2026**, *16*, 498. [CrossRef]
31. Wang, J.; Liu, Y.; Liu, D.; Mu, Y.; Jia, X. Strong Radiative Cooling Coating Containing In Situ Grown TiO_2/CNT Hybrids and Polyacrylic Acid Matrix. *Coatings* **2025**, *15*, 921. [CrossRef]
32. Wang, D.; Ma, Y.; Ma, Y.; Liu, B.; Sun, D.; Ran, Q. Foamy Melamine Resin–Silica Aerogel Composite-Derived Thermal Insulation Coating. *Nanomaterials* **2025**, *15*, 135. [CrossRef] [PubMed]
33. Wang, F.; Du, J.; Hu, X.; Li, X.; Song, J.; Li, C.; Li, J.; Li, L.; Yang, L.; Xu, Z. Zero-energy solution for thermal cracking to concrete: High-altitude anti-cracking coating based on radiative cooling. *Sci. China Technol. Sci.* **2025**, *68*, 1720102. [CrossRef]
34. Xue, J.; Liu, L.; Meng, Y.; Chen, Z.; Yang, Y. Constructing powerful interface between glass fiber and silica aerogel via an interfacial molecular bridge allows for excellent acoustic-thermal insulation composites. *Constr. Build. Mater.* **2025**, *465*, 140260. [CrossRef]
35. Lei, Y.; Zheng, Q.; Zhu, H.; Dou, R.; Yuan, J.; Zhao, Y.; Peng, H.; Yu, P. A novel thermal insulation and anticorrosion coating based on silica aerogel modification for mild steel: Experimental and theoretical studies. *Mater. Today Commun.* **2024**, *41*, 111105. [CrossRef]
36. Long, H.; Lei, S.; Wang, F.; Yang, S.; Ju, H.; Ou, J. Superhydrophobic daytime radiative cooling coating incorporated with phase change microcapsules for building thermal regulation. *J. Mater. Sci.* **2024**, *59*, 6459–6475. [CrossRef]
37. He, H.; Zhao, Q.; Chen, B.; Zhang, Z.; Zhang, N.; Attia, S.; Yuan, Y.; Wołoszyn, J. All-weather passive building thermal management: Design and performance evaluation of radiative cooling coating integrated with phase change materials. *Appl. Therm. Eng.* **2026**, *298*, 130933. [CrossRef]
38. Gao, J.; Zhan, Y.; Fan, C. Selection of ideal emissivity spectrum for radiative cooling and its application in water harvesting. *Int. J. Heat Mass Transf.* **2024**, *231*, 125868. [CrossRef]

Disclaimer/Publisher's Note: The statements, opinions and data contained in all publications are solely those of the individual author(s) and contributor(s) and not of MDPI and/or the editor(s). MDPI and/or the editor(s) disclaim responsibility for any injury to people or property resulting from any ideas, methods, instructions or products referred to in the content.